Strength of sapphire as a function of temperature and crystal orientation

John W. Fischer,* W. R. Compton,† Nancy A. Jaeger,† and Daniel C. Harris*

*Chemistry Division, Research Department
†Missile Airframe Division, Attack Weapons Department
Naval Weapons Center, China Lake CA, 93555-6001

ABSTRACT

The strengths of sapphire disks of two different crystallographic orientations and bars of three different orientations were measured as a function of temperature in ring-on-ring flexure or 4-point bending. One set of disks (0° cut) had the crystallographic *c* -axis normal to the flat surface which contained the crystallographic *a*- and *m*-axes. The average strength of these disks dropped from 154 ksi at 20°C to 21 ksi at 800°C. In another set of disks (90° cut), the crystallographic *c*- and *m*-axes were parallel to the flat surface. The average strength of these disks dropped from 84 ksi at 20°C to 48 ksi at 800°C. The strength of sapphire bars whose tensile axis was the crystallographic *m* axis dropped from 103 ksi at 20°C to 86 ksi at 1400°C. The strength of sapphire bars whose tensile axis was the crystallographic *a*-axis dropped from 113 ksi at 20°C to 74 ksi at 1400°C. The strength of sapphire bars whose tensile axis was the crystallographic *c*-axis dropped from 153 ksi at 20°C to 35 ksi at 1400°C.

1. INTRODUCTION

Single-crystal sapphire is a strong, hard optical material with good thermal shock resistance, low optical scatter, and excellent transmission at wavelengths between 0.15 and 5-μm.[1-3] Recent advances in manufacturing technology promise to reduce the cost of high quality material.[4,5] The strengths of sapphire fibers,[6-11] single crystals of various orientations,[12-16] and polycrystalline material[14] have been measured previously as a function of temperature, but adequate data for engineering design with bulk single-crystal sapphire is lacking. Two studies of sapphire filaments whose long axis is the crystal *c*-axis found tensile strengths of approximately 280[11] and 380[6] ksi (ksi = 1000 lbs/in^2) at 20°C. There is an initial sharp drop in strength to a minimum in the region 250-600°C, an increase of strength up to 900-1000°C and then another decrease of strength at higher temperature.[11] *a*-Axis sapphire filaments had similar strength and temperature-dependence of strength as *c*-axis fibers.[7] Four measurements[12-16] of the flexure strength of bulk single-crystal sapphire of various orientations gave strengths at 20°C in the range 20-120 ksi. Two studies of the temperature dependence of this strength showed a minimum in the 300-600°C range,[14,15] A third study showed decreasing strength from 20 to 250 to 500°C[16] for one crystal orientation, while a fourth study noted decreasing strength from 20 to 500 to 1000°C for two different crystal orientations.[12] The strength of polycrystalline alumina was constant from 20-800°C before gradually decreasing at higher temperatures.[14] The design minimum tensile strength of Czochralski-grown sapphire is listed by one manufacturer as 58 ksi at 20°C, 40 ksi at 500°C, and 52 ksi at 1000°C.[17] The present work was undertaken to provide flexure strength data as a function of temperature and crystal orientation for bulk single-crystal sapphire with a representative optical finish scratch/dig specification of 60/40.

Approved for public release; distribution is unlimited.

2. SPECIMENS

Sapphire obtained from Crystal Systems (Salem, Mass.) was grown by the Schmid-Viechnicki method and polished to a nominal scratch/dig specification of 60/40 using a random circular motion. Flexure testing was carried out at the University of Dayton Research Institute, Wright-Patterson Air Force Base, Ohio, with an Instron Model 1123 Universal Testing Machine at a crosshead speed of 0.508 mm/min at the specified temperatures. Bend bars with dimensions 45 x 4 x 3 mm were subjected to 4-point flexure testing using loads separated by 10 mm and supports separated by 40 mm on the 45 x 4 mm faces. The long edges of the bars were rounded to a radius of 0.08-0.13 mm and polished using a random circular motion. Ring-on-ring biaxial flexure testing of 2-mm-thick disks with a diameter of 38 mm was performed with a load ring radius of 7.937 mm and a support ring radius of 15.875 mm.

Figure 1a designates various faces of a sapphire crystal and Fig. 1b provides a view down the 3-fold symmetry c-axis of the crystal. The crystallographic *a*-axis in Fig. 1b is a 2-fold symmetry axis. The *m*- and *c* -axes in Fig. 1a define a mirror symmetry plane. Five types of specimens were prepared for flexure testing. Figure 2 shows a bend bar in which tension will be directed along the *m*-axis, with the *c*-axis perpendicular to the tensile face. In Figs. 3 and 4 the tensile axes are the crystallographic *c*- and *a*-axes, respectively. Figures 5 and 6 show two orientations of disks used for ring-on-ring biaxial flexure testing. In one case (called a 0° cut) the *c*-axis is perpendicular to the disk face and in the other case (called a 90° cut) the disk face is the *a*-plane containing the *c*- and *m*-axes.

3. STRESS ANALYSIS

Stress levels at fracture for the 4-point flexure bar specimens were computed from simple beam theory as

$$\sigma_u = \frac{9PL}{8wt^2} \tag{1}$$

where σ_u is the maximum stress on the tensile surface of the bar, P is the applied load, w is the width of the bar, t is the thickness of the bar, and L is the length of the bar between supports. The stress on the tensile surfaces of the bar varies linearly from this maximum value to zero at the supports in the longitudinal direction (bottom of the bar) and at the bar neutral axis in the bar thickness direction (sides of the bar).

Flexure strength measurements reported later in this paper indicate that the strength of sapphire in the crystallographic *a* direction is similar to the strength in the *m* direction. Therefore, stress levels at fracture for disks with the *c*-axis normal to the flat surface were computed from Equation 2, which applies to an equibiaxial stress field.[18,19]

$$\sigma_u = \frac{3P}{(4\pi t^2)}\left\{\left[2(1+\nu)\ln\left(\frac{a}{b}\right)\right] + \left[(1-\nu)\left(\frac{a}{R}\right)^2\right]\left[1-\left(\frac{b}{a}\right)^2\right]\right\} \tag{2}$$

where σ_u is the maximum equibiaxial stress on the tensile surface of a disk of thickness (t) inside of the load ring radius (b) where the applied load is P and ν is Poisson's ratio. The disk has outside radius (R) and is supported on a ring of radius (a). The corresponding stress levels for a point on the tensile surface outside of the load radius, b, are given by the equations

$$\sigma_{ur} = \frac{3P}{(4\pi t^2)}\left\{\left[2(1+\nu)\ln\left(\frac{a}{r}\right)\right]+\left[(1-\nu)\left(\frac{a}{R}\right)^2\right]\left[\left(\frac{b}{r}\right)^2-\left(\frac{b}{a}\right)^2\right]\right\} \quad (3)$$

$$\sigma_{ut} = \frac{3P}{(4\pi t^2)}\left\{\left[2(1+\nu)\ln\left(\frac{a}{r}\right)\right]+\left[(1-\nu)\left(\frac{a}{R}\right)^2\right]\left[2-\left(\frac{b}{r}\right)^2-\left(\frac{b}{a}\right)^2\right]\right\} \quad (4)$$

where σ_{ur} is the local radial component of stress and σ_{ut} is the local hoop component of stress at radial position (r).

Stress levels at fracture for disk specimens with the *c*-axis parallel to the flat surface of the disk were derived from a finite element model using the ABAQUS[20] computer program and the orthotropic material properties shown in Tables 1 and 2. An orthotropic model was used in the analysis because of crystal symmetry. The modulus data shown in Table 1 were used to derive the linear elasticity matrix coefficients shown in Table 2. A 90° segment of the flexure disk geometry was subdivided into 1800 finite elements (Fig. 7). The disk segment was simply supported at radial location, a, and a load of P/4 was distributed along the curve, r = b. The edges of the disk segment parallel to and intersecting at the disk axis of symmetry were constrained to zero rotation about the disk radius.

4. FRACTURE STATISTICS

The survival of a brittle material subjected to a general biaxial stress state at its surface has been described statistically by Batdorf[21] as

$$\ln P_s = -\int dA \int \frac{\omega}{\pi}\frac{dN}{d\sigma_c}\, d\sigma_c \quad (5)$$

where P_S is the probability that an elemental area, A, will survive with a critical crack strength of σ_C if the probability that such a crack is present in the material surface is $dN/d\sigma_C$, and when the probability that the crack is facing a direction that will permit fracture is ω/π. This equation may be restated in a more convenient computational form as follows:

$$\ln P_s = \int \frac{2m}{\pi}\left[\frac{\sigma_z}{\sigma_o}\right]^m \int_0^1 \theta_c K_c^{m-1}\, dK_c\, dA \quad (6)$$

where $K_C = \sigma_C/\sigma_Z$, $\omega/\pi = 2\theta/\pi$, m is the Weibull modulus, σ_o is the Weibull scaling parameter, σ_z is the principal stress in the z-direction and θ_c and ϕ_c are critical crack orientation angles defined in Fig. 8. The critical surface crack orientation angles are determined from a root of the equation,

$$G\left(K_x, K_y, K_a, K_b, K_c, \phi_c, \theta_c\right) = \frac{2\sigma_u}{\sigma_z} - \frac{2\sigma_e}{\sigma_z} = 0 \quad (7)$$

where σ_x is the stress component in the x-direction (Fig. 8), σ_y is the stress component in the y-direction, σ_e is the effective stress applied at the tip of a crack, σ_u is the crack strength. The remaining variables in Equation 7 are defined below.

$$K_x = \frac{\sigma_x}{\sigma_z}\ ,\quad K_y = \frac{\sigma_y}{\sigma_z}\ ,\quad K_a = \frac{\sigma_{um}}{\sigma_{ua}}\ ,\quad K_b = \frac{\sigma_{uc}}{\sigma_{uB}} \quad (8)$$

and $$\sigma_{uB} = \sigma_{ua}\left\{1 - \left[1 - K_a\right]\cos^2(3\phi)\right\} \tag{9}$$

where σ_{um} is the average flexure strength with the tensile axis along the *m*-axis, σ_{ua} is the average flexural strength with the tensile axis along the *a*-axis, and σ_{uc} is the average flexural strength with the tensile axis along the *c*-axis. Finally, the two terms on the right side of Equation 7 are defined by the relations

$$\frac{2\sigma_e}{\sigma_z} = a_1\left[\left(K_x\cos^2\phi + K_y\sin^2\phi\right)\sin^2\theta + \cos^2\theta\right] +$$

$$\left\{a_2\left[\left(K_x\cos^2\phi + K_y\sin^2\phi\right)\sin^2\theta + \cos^2\theta\right]^2 + a_3\left[1 - K_x\cos^2\phi - K_y\sin^2\phi\right]^2\sin^2\theta\cos^2\theta\right\}^{\frac{1}{2}} \tag{10}$$

and

$$\frac{2\sigma_u}{\sigma_z} = \frac{2\sigma_{uc}}{\sigma_z\sqrt{\cos^2\theta + K_b^2\sin^2\theta}} \tag{11}$$

where $a_1 = 0$, $a_2 = (1.1215)^2$, and $a_3 = (1/(1\text{-}0.5\nu)^2$ are constants derived from strain energy release rate relations for a penny-shaped surface crack.[22]

The probability of survival of a particular flexure specimen was determined by first subdividing the tensile surface of the flexure specimen into elemental areas and then computing the probability of survival for each of these elemental areas. The product of the individual area element probabilities of survival was then the approximate probability of survival of the flexure specimen. The Weibull parameters, σ_o and m, were then determined by minimizing the absolute error between the predicted and experimental probabilities of failure ($P_f = 1 - P_s$) for the flexure specimen tensile surfaces using the *Downhill Simplex* method.[23]

5. RESULTS

Although 40 bars were tested at each temperature, approximately half of the results above 20°C were discarded because fracture appeared to occur at the load or support positions. All of the bar data collected at 20°C were acceptable and all of the disk data collected at 20 and 800°C were considered valid. Figures 9-13 present the variation of flexure strength with temperature for the specimens in Figs. 2-6. The vertical bars are standard deviations. Table 3 presents a summary of the average flexure strength (σ_u), Weibull statistics (m and σ_o) and strength ratios (K_a and K_b in Equation 8) for both the uniaxial bar and the biaxial disk specimens. The first set of *m*-axis tensile bars in Table 3 has only 34 results because six specimens were tested with a different load span from the rest. Figures 14-16 present a comparison of the experimental probabilities of failure and the best fit obtained from Batdorf's theory for the 4-point uniaxial flexure tests at 20°C.

The filled squares in Fig. 17 are experimental results for the disks in Fig. 5 tested at 20°C. The open squares (and solid line) are from the best fit biaxial analysis. The triangles in Fig. 17 show the expected behavior of these disks when the uniaxial constants from the *a*-axis and *m*-axis 4-point bend specimens are used to predict the probability of failure. The uniaxial results predict a higher probability of failure at a given stress than is observed in the biaxial case. The bars, therefore, give a conservative prediction for the disks. Figure 18 gives the corresponding results for the disks in Fig. 6 tested at 20°C. In this case, the

uniaxial results predict a slightly lower probability of failure than is actually observed for the disks.

6. DISCUSSION

The biaxial flexure strengths reported in Table 3 for the disks in Fig. 5 (0° cut) are consistent with a previous report[12] in which the strength of 50.8-mm-diameter disks with a thickness of 2.54 mm dropped from 102 ksi at 20°C to 50 ksi at 500°C and 22 ksi at 1000°C. We observe a decrease in strength from 154 ksi at 20°C to 21 ksi at 800°C for stress in the plane of the *a*- and *m*-crystallographic axes. In contrast, the disks in Fig. 6, for which tensile stress is applied in the plane of the *c*- and *m*-axes, decreases from 84 ksi at 20°C to 48 ksi at 800°C. Taken together, these two sets of results imply that *c*-axis strength is less than *a* and *m*-axis strength at 20°C, but that *c*-axis strength does not decrease as much as *a*- and *m*-axis strength when the temperature is raised to 800°C.

The 4-point bending results in Table 3 show that the strength in the direction of the *a*-axis is essentially equal to the strength along the *m*-axis. The 4-point uniaxial flexure results are not consistent with the biaxial flexure strengths. The bars show that the *c*-axis is the strongest at 20°C, whereas the disks imply that the *c*-axis is the weakest. The bars show that the strength drops the most along the *c*-axis as the temperature is raised, whereas the disks show the least drop for *c*-axis strength.

When the Weibull constants derived from 20°C uniaxial flexure tests are applied to the 20°C biaxial flexure test data (*c*-axis normal to tensile surface), the theory conservatively predicts a higher probability of failure at a particular stress level than observed experimentally (Fig. 17). The theory significantly underpredicts the probability of failure when the Weibull constants derived from 500-1000°C uniaxial flexure tests are applied to the 800°C biaxial flexure test data for the same crystal orientation.

Application of Weibull constants derived from 20°C uniaxial flexure tests to the 20°C biaxial flexure tests which had the crystal *m*-axis and *a*-axis parallel to the tensile surface slightly underpredict the observed probability of failure (Fig. 18). In this instance the theory again underpredicts the probability of failure when the Weibull constants derived from 500-1000°C uniaxial flexure tests are applied to the 800°C biaxial flexure test data for the same crystal orientation.

Sapphire window and dome temperatures in typical thermal shock applications are normally less than 500°C. For these applications, it is recommended that the strengths and biaxial fracture statistics shown in Table 3 for 20°C be used in conjunction with a stress analysis to predict the probability of failure for the sapphire component. The uniaxial and biaxial results at elevated temperatures in Table 3 are contradictory and should be used with caution in the absence of further experiments.

7. REFERENCES

1. R. L. Gentilman, "Current and Emerging Materials for 3-5 Micron IR Transmission," *Proc. SPIE, 68,* 2-11 (1986).
2. S. Musikant, *Optical Materials,* Marcel Dekker, New York, 1985.
3. J. A. Savage, *Infrared Optical Materials and their Antireflection Coatings,* Adam Hilger, Bristol, 1985.
4. F. Schmid and C. P. Khattak, "Current Status of Sapphire Technology for Window and Dome Applications," *Proc. SPIE, 1112,* 25-30 (1989).
5. H. E. LaBelle, J. Serafino and J. J. Fitzgibbon, "Recent Developments in Growth of Shaped Sapphire Crystals," *Proc. SPIE, 683,* 36-40 (1986).

6. H. E. LaBelle, Jr. and G. F. Hurley, "Strength and Fracture of Long Single Crystal Sapphire Filaments," *SAMPE J., 6,* 17-35 (1970).
7. G. F. Hurley, "Mechanical Behavior of Melt-Grown Sapphire at Elevated Temperature," *Applied Polymer Symposium, 21,* 121-130 (1973).
8. R. L. Crane, "An Investigation of the Mechanical Properties of Silicon Carbide and Sapphire Filaments," Air Force Materials Laboratory, Wright-Patterson Air Force Base, Report No. AFML-TR-72-180, 1972.
9. J. T. A. Pollock and G. F. Hurley, "Dependence of Room Temperature Fracture Strength on Strain-Rate in Sapphire," *J. Mater. Sci., 8,* 1595-1602 (1973).
10. D. M. Kotchick and R. E. Tressler, "Surface Damage and Environmental Effects on the Strain-Rate Sensitivity of the Strength of Sapphire and Silicon Carbide Filaments," *J. Mater. Sci., 10,* 608-612 (1975).
11. R. L. Crane and R. E. Tressler, "Effect of Surface Damage on the Strength of C-Axis Sapphire Filaments," *J. Composite Mater., 5,* 537-541 (1971).
12. R. L. Gentilman, E. A. Maguire, H. S. Starrett, T. M. Hartnett and H. P. Kirchner, "Strength and Transmittance of Sapphire and Strengthened Sapphire," *Commun. Am. Cer. Soc.,* C116-C117 (1981).
13. P. F. Becher, "Fracture-Strength Anisotropy of Sapphire," *J. Am. Cer. Soc., 59,* 59-61 (1976).
14. E. A. Jackman and J. P. Roberts, "The Strength of Single Crystal and Polycrystalline Corundum," *Phil. Mag., 46,* 809-811 (1955).
15. J. B. Wachtman, Jr. and L. H. Maxwell, "Strength of Synthetic Single Crystal Sapphire and Ruby as a Function of Temperature and Orientation," *J. Am. Cer. Soc., 42,* 432-433 (1959).
16. J. A. Cox, D. Greenlaw, G. Terry, K. McHenry and L. Fielder, "Comparative Study of Advanced IR Transmissive Materials," *Proc. SPIE, 683,* 49-62 (1986).
17. Union Carbide materials data cited in reference 2.
18. F. F. Vitman and V. P. Pukh, "A Method for Determining the Strength of Sheet Glass," *Zavod Lab.,* 29 [7] 863-67 (1963).
19. S. Timoshenko and S. Woinowsky-Kneger, *Theory of Plates and Shells,* 2nd ed., p 51, McGraw-Hill, New York (1959).
20. *ABAQUS USER'S MANUAL Vers 4.8,* Hibbitt, Karlsson and Sorensen, Inc. (1989).
21. S. B. Batdorf and D. J. Chang, "On the relation between the fracture statistics of volume distributed and surface distributed cracks," *UCLA-ENG-7723* (1977).
22. B. Paul and L. Mirandy, "An Improved Fracture Criterion fot Three Dimensional Stress States," *Trans. ASME* 98, 159 (1975).
23. J. A. Nelder and R. Mead, *Computer Journal,* 7,308 (1965).
24. F. A. Strobel,"Thermostructural Evaluation of Four Seeker Dome Materials, Part 1. Test and Analysis," Naval Weapons Center Technical Publication 6539, Table C-9, (April 1985).

Table 1. Young's Modulus of Sapphire.[24]

T (°C)	$E_{c\text{-}axis}$ (10^6 psi)	$E_{a\text{-}axis}$ (10^6 psi)	$E_{m\text{-}axis}$ (10^6 psi)
20	63.3	55.8	55.8
815	59.4	52.4	52.4
1095	55.5	48.9	48.9

Table 2. Orthotropic Elasticity Matrix Constants.

Temp (°C)	C_{1111} (10^6psi)	C_{1122} (10^6psi)	C_{2222} (10^6psi)	C_{1133} (10^6psi)	C_{2233} (10^6psi)	C_{3333} (10^6psi)	C_{1212} (10^6psi)	C_{1313} (10^6psi)	C_{2323} (10^6psi)
20	76.826	25.048	68.355	25.048	24.418	68.355	24.920	24.920	21.969
815	72.104	23.526	64.196	23.526	22.936	64.196	23.390	23.390	20.630
1095	67.352	21.949	59.898	21.949	21.394	59.898	21.850	21.850	19.252

Poisson Ratio = ν = 0.27. Moduli are assumed to be constant above 1093°.

$$\begin{pmatrix}\sigma_{11}\\ \sigma_{22}\\ \sigma_{33}\\ \tau_{12}\\ \tau_{13}\\ \tau_{23}\end{pmatrix} = \begin{bmatrix} C_{1111} & C_{1122} & C_{1133} & C_{1112} & C_{1113} & C_{1123} \\ & C_{2222} & C_{2233} & C_{2212} & C_{2213} & C_{2223} \\ & & C_{3333} & C_{3312} & C_{3313} & C_{3323} \\ & \text{symm.} & & C_{1212} & C_{1213} & C_{1223} \\ & & & & C_{1313} & C_{1323} \\ & & & & & C_{2323} \end{bmatrix} \begin{pmatrix}\varepsilon_{11}\\ \varepsilon_{22}\\ \varepsilon_{33}\\ \gamma_{12}\\ \gamma_{13}\\ \gamma_{23}\end{pmatrix}$$

$\sigma_{11}, \sigma_{22}, \sigma_{33}$ = direct stress in 1,2,3 directions

$\tau_{12}, \tau_{13}, \tau_{23}$ = shear stress in the 12, 13, 23 planes

ε and γ are the respective strains

Table 3. Summary of Sapphire Flexure Strength and Batdorf Fracture Statistics.

Tensile Axis	T (°C)	No. of Spec*	σ_o (ksi)	m	K_a	K_b	σ_u† (ksi)	Std Dev (ksi)
m	20	34	70.28	4.00	0.904	1.494	103	29
(Fig. 2)	500	12	83.34	3.78	0.992	0.705	122	32
	1000	14	68.55	13.7	0.769	0.321	76	6
	1400	18	72.06	7.81	1.164	0.407	86	11
a	20	40	74.92	3.59	0.904	1.494	114	34
(Fig. 3)	500	20	73.34	2.09	0.992	0.705	123	54
	1000	2	...	...	...	...	99	...
	1400	13	62.72	8.55	1.164	0.407	74	8
c	20	40	108.49	3.28	0.904	1.494	153	50
(Fig. 4)	500	39	60.02	4.31	0.992	0.705	86	22
	1000	40	16.48	4.37	0.769	0.321	25	59
	1400	38	22.81	3.90	1.164	0.407	35	10
a and *m*	20	20	151.46	3.39	0.904	1.494	154	48
(Fig. 5)	800	20	20.12	14.7	0.858	0.475	21	2
c and *m*	20	20	53.94	3.31	0.904	1.494	84	24
(Fig. 6)	800	20	19.60	2.30	0.858	0.475	48	21

*A total of 40 uniaxial or 20 biaxial specimens were broken at each temperature
†Average flexure strength of the number of specimens indicated

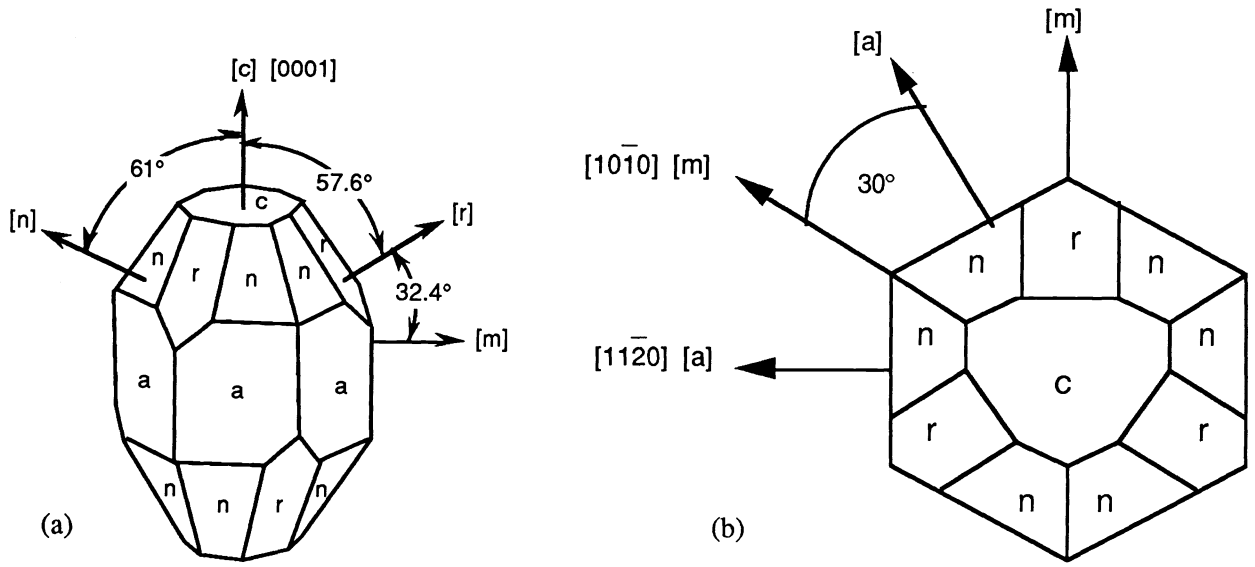

Figure 1. (a) Side view of sapphire crystal showing mineralogical designations of faces and (b) view down 3-fold crystallographic *c*-axis.

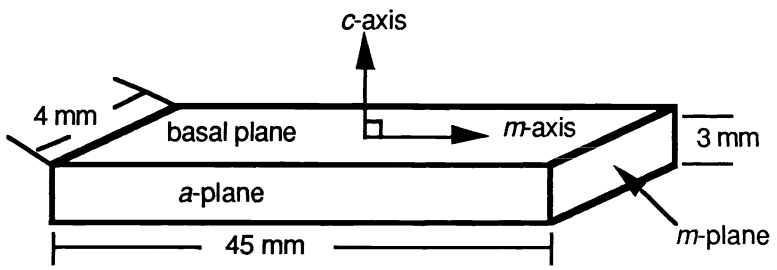

Figure 2. Sapphire bend bar with *c*-axis perpendicular to tensile surface and tension directed along the *m*-axis.

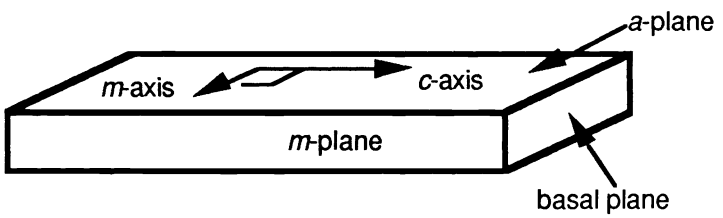

Figure 3. Sapphire bend bar with tensile face defined by the *c*- and *m*-axes and tension directed along the *c*-axis.

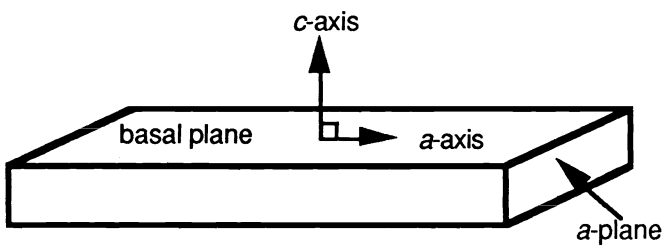

Figure 4. Sapphire bend bar with *c*-axis perpendicuar to tensile surface and tension directed along the *a*-axis.

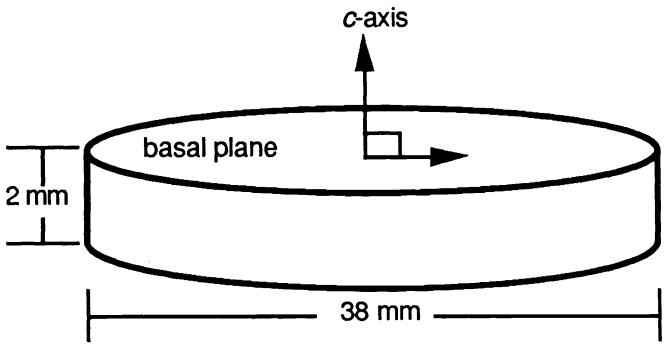

Figure 5. Sapphire disk with the tensile surface perpendicular to the *c*-axis.

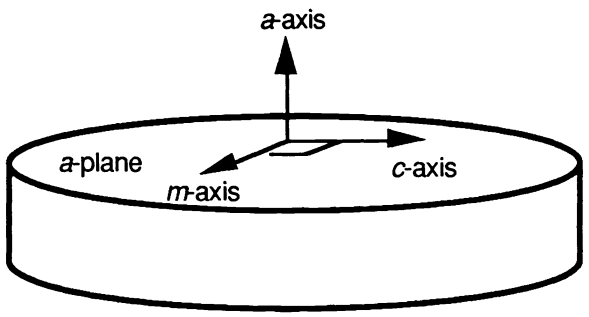

Figure 6. Sapphire disk with the tensile surface defined by the *a*- and *m*-axes.

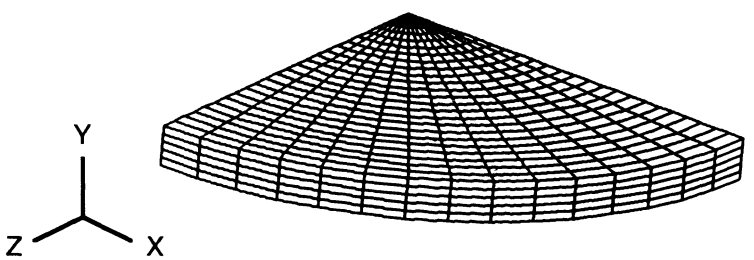

Figure 7. Finite element model of flexure test disk.

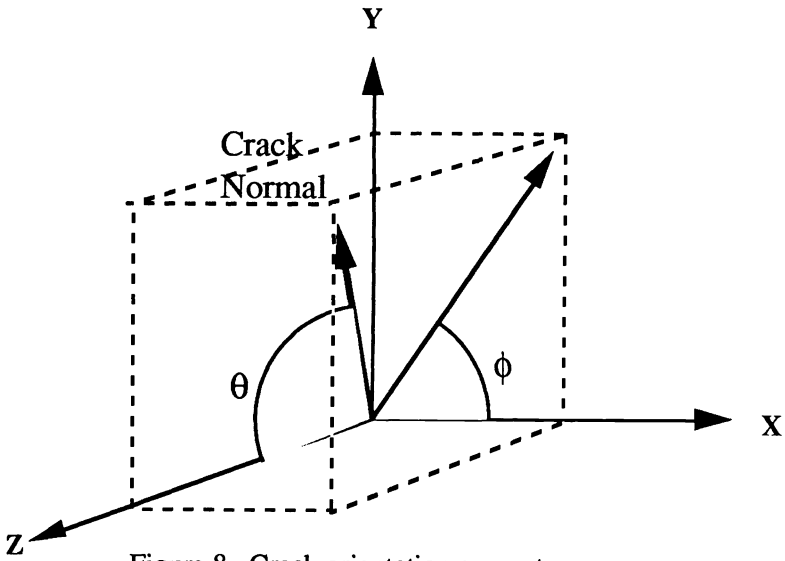

Figure 8. Crack orientation geometry.

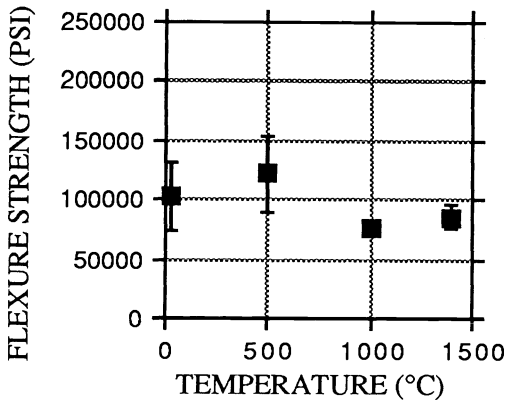

Figure 9. Variation of *m*-axis flexure strength with temperature.

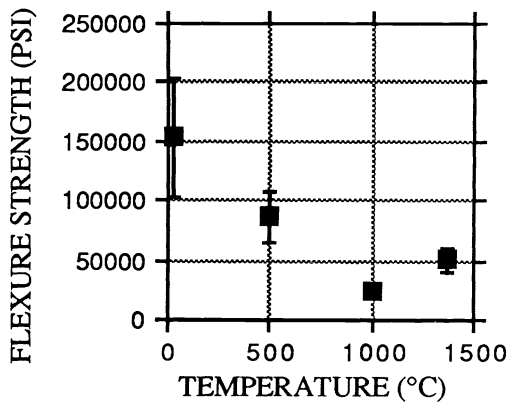

Figure 10. Variation of *c*-axis flexure strength with temperture.

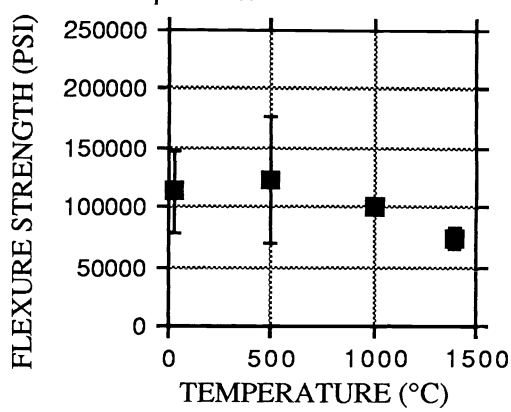

Figure 11. Variation of *a*-axis flexure strength with temperature.

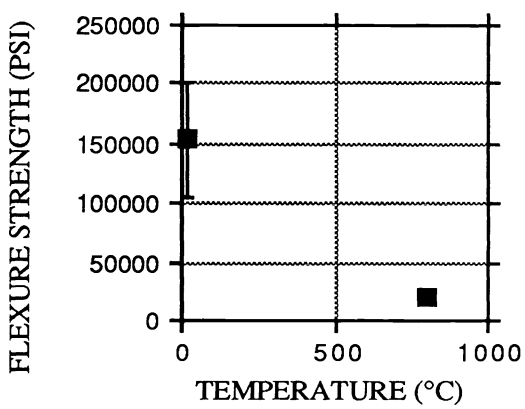

Figure 12. Variation of biaxial flexure strength with temperature (*a*-axis and *m*-axis in tensile surface.

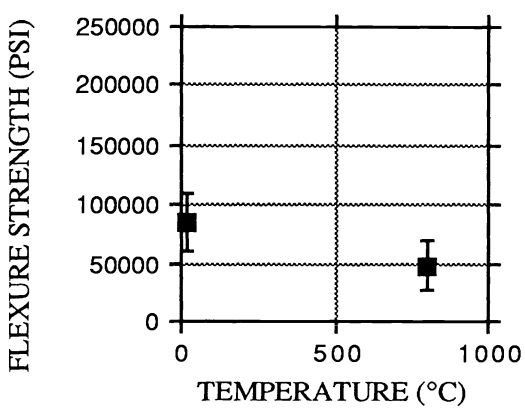

Figure 13. Variation of biaxial flexure strength with temperature (c-axis and m-axis in tensile surface.

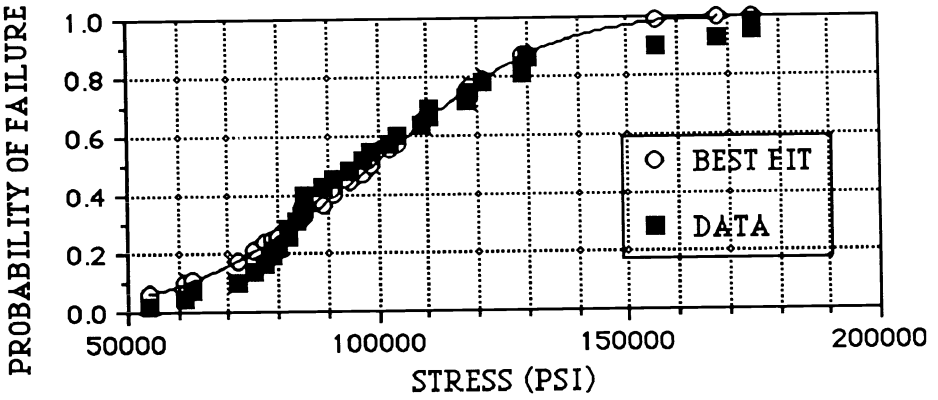

Figure 14. *m*-Axis uniaxial probability of failure (20°C).

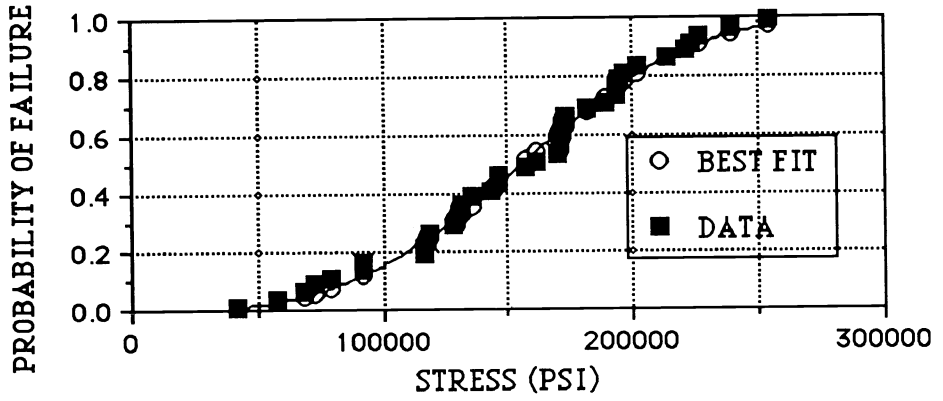

Figure 15. *c*-Axis uniaxial probability of failure (20°C).

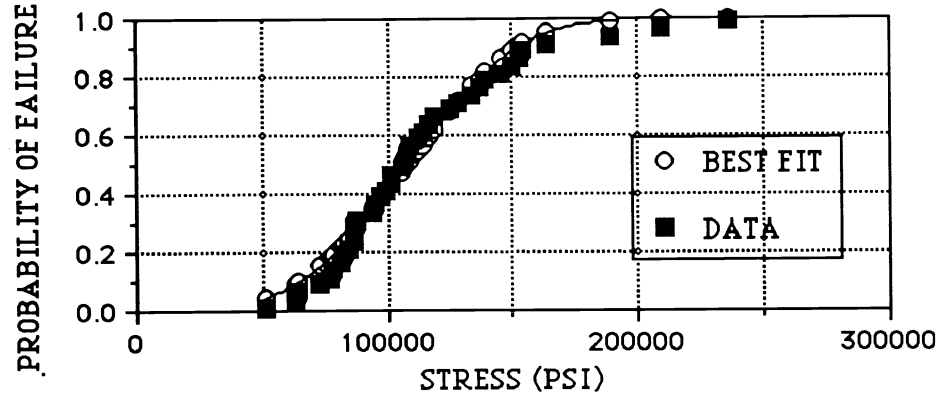

Figure 16. *a*-Axis uniaxial probability of failure (20°C).

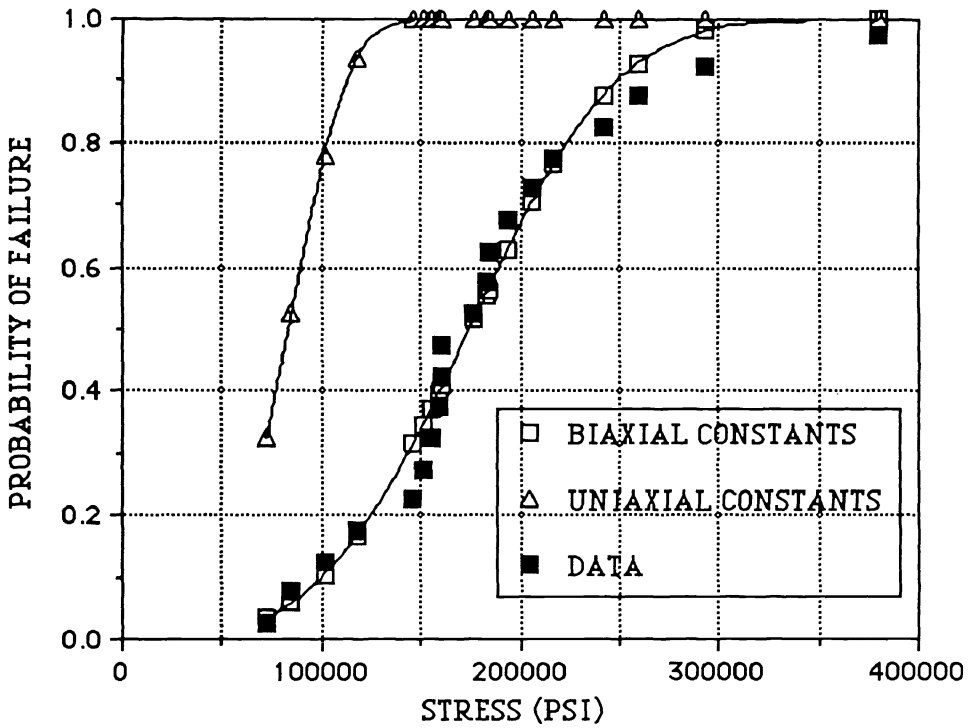

Figure 17. *a*-Axis/*m*-axis biaxial probability of failure (20°C).

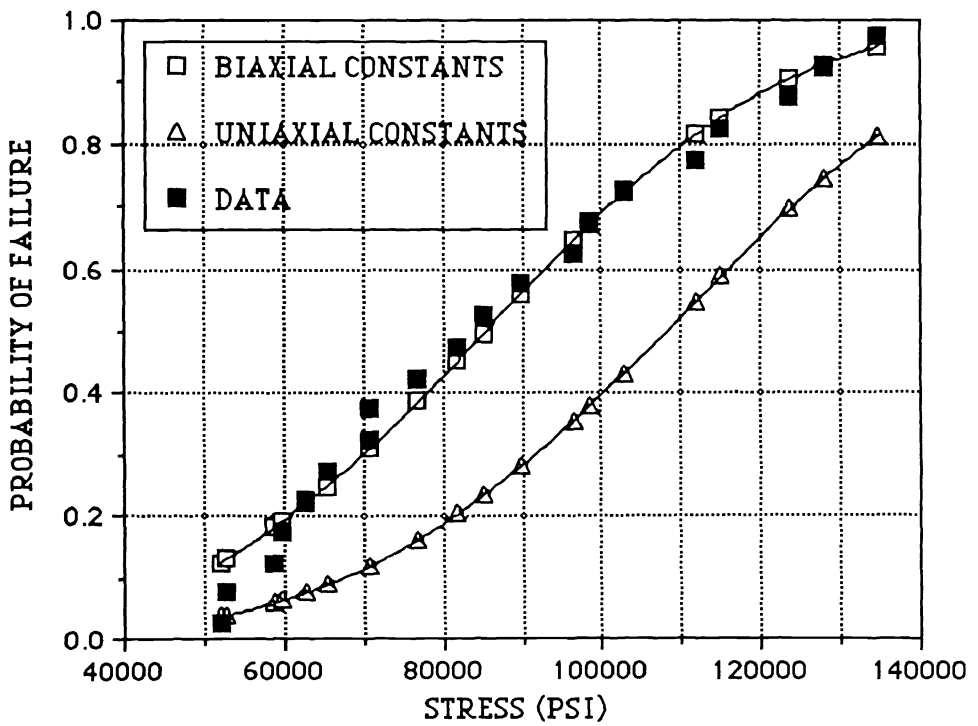

Figure 18. *c*-Axis/*m*-axis biaxial probability of failure (20°C).